Energy & Environmental Science

PAPER

View Article Online
View Journal | View Issue

Cite this: *Energy Environ. Sci.*, 2015, **8**, 2970

Photochemical charge transfer observed in nanoscale hydrogen evolving photocatalysts using surface photovoltage spectroscopy†

J. Wang, J. Zhao and F. E. Osterloh*

Received 1st June 2015,
Accepted 13th July 2015

DOI: 10.1039/c5ee01701g

www.rsc.org/ees

The application of inorganic nanostructures for solar water splitting is currently limited by our understanding of photochemical charge transfer on the nanoscale, where space charge layers are less effective for carrier separation. Here we employ surface photovoltage spectroscopy to measure the internal photovoltages in single crystalline platinum/ruthenium-modified Rh-doped $SrTiO_3$ nanocrystals for the first time. Voltages of −0.88 V and −1.13 V are found between the absorber and the Ru and Pt cocatalysts, respectively, and a voltage of −1.48 V for a Rh:$SrTiO_3$ film on an Au substrate. This shows that the Pt and Ru cocatalysts not only improve the redox kinetics but also aid charge separation in the absorber. Voltages of +0.4 V, +0.6 V, and +1.2 V are found for hole injection into KI, $K_4[Fe(CN)_6]$, and methanol, respectively, and a voltage of −0.7 V for electron injection into $K_3[Fe(CN)_6]$. These voltages correlate well with the photocatalytic performance of the catalyst; they are influenced by the built-in potentials of the donor-acceptor configurations, the physical separation of donors and acceptors, and the reversibility of the redox reaction. The photovoltage data also allowed the identification of a photosynthetic system for hydrogen evolution (80 μmol g^{-1} h^{-1}) under visible light illumination (>400 nm) from 0.05 M aqueous $K_4[Fe(CN)_6]$.

Broader context

Nanostructured light absorbers have advantages for solar water splitting, including shortened carrier collection pathways and improved light distribution. However, the application of nanoscale absorbers for artificial photosynthesis is currently limited by our understanding of photochemical charge transfer on the nanoscale, where space charge layers are not effective for charge separation. Here we employ surface photovoltage spectroscopy (SPS) to observe electron and hole transfer from single crystalline platinum/ruthenium-modified Rh-doped $SrTiO_3$ nanocrystals for the first time. We find that the absorber-Pt/Ru junctions promote electron-hole separation strongly, allowing open circuit voltages of over 1.0 V. This is comparable to the effect of molecular redox reagents at the absorber surfaces. Overall, we find that nanoscale charge transfer is controlled by the built-in potentials of the absorber/acceptor configuration, by the spatial separation between donors and acceptors and by the reversibility of the redox reactions. These observations aid the understanding of photochemical charge transfer on the nanoscale and contribute to the design of more efficient systems for artificial photosynthesis.

Introduction

Solar water photoelectrolysis with suspended photocatalysts is regarded as the most direct and inexpensive avenue to sustainable fuels from solar energy.[1–9] The efficiency of such catalysts is currently limited by our understanding of charge separation on the nanoscale.[5,10,11] On the nanoscale, space charge layers are no longer effective, and the kinetics of photochemical charge transfer and the corresponding junction potentials are controlled by states at solid–solid and solid–liquid interfaces.[12,13] These junction potentials are difficult to probe with electrochemical methods because of the coupling of charge transfer with Faradaic processes at the solid–liquid interface. The overpotentials associated with the Faradic processes are generally unknown[14,15] or require specialized techniques for measurement.[16] Furthermore, charge transfer through films is slow and associated with a current dependent Ohmic potential drop across the films.[17,18] These two effects obscure the true photovoltage at nanoparticle interfaces. Here we demonstrate that solid–solid and solid–liquid junction potentials at nanoparticle interfaces can be directly measured with surface photovoltage spectroscopy (SPS).[19,20] In SPS a contactless Kelvin Probe probes the formation of photodipoles in a capacitive arrangement without the limitations of charge transfer resistance. The higher sensitivity allows the

Department of Chemistry, University of California, Davis, One Shields Avenue, Davis, CA 95616, USA. E-mail: fosterloh@ucdavis.edu

† Electronic supplementary information (ESI) available: Powder X-ray diffraction patterns, spectra of the SPS light source, sample configuration, H_2 evolution data, UV/Vis absorbance spectra, and calculation of the electron and hole diffusion lengths for $SrTiO_3$. See DOI: 10.1039/c5ee01701g

observation of localized charge transfer states with small optical cross sections.[17,21–28] As a model system we use single crystalline nanoparticles of Rh-doped $SrTiO_3$. $SrTiO_3$ is an established photocatalyst for overall water splitting under UV light only,[18,21,29–31] but it can be converted into a visible light responsive material upon doping with Cr,[32] Cr/Sb,[33,34] Cr/Ta,[35] Rh,[36,37] Ni/Ta,[38] and Cr/La.[39] These materials have been shown to catalyze the hydrogen evolution reaction (HER) and the oxygen evolution reaction (OER) in the presence of sacrificial agents and under visible light.[33,37] The Rh and Cr-doped systems have also been successfully employed as photocathodes in Type 2 Tandem devices for the overall water splitting reaction.[1,40–42] There, coupling to the tandem absorber is either established *via* direct physical contact or *via* soluble redox couples, such as $Fe^{3+/2+}$.[40,43] Even though photocatalytic reactions of Rh:$SrTiO_3$ microparticles have been reported in the presence of these redox couples[44–46] or with $BiVO_4$,[40,41] no quantitative electrochemical information on junction potentials is available. As we show here, significant photopotentials can be generated at the interfaces between Rh:$SrTiO_3$ nanocrystals when in contact with Pt or Ru nanoparticles or molecular redox couples. Measurement of these potentials is key to the optimization of artificial photosynthesis with nanostructures and to the identification of novel fuel-forming photochemical reactions.[1,4,5,47,48] As an example, we use the photovoltage data here to establish visible light driven photosynthetic hydrogen evolution using ferrocyanide as a sacrificial donor for Rh:$SrTiO_3$ for the first time.

Results and discussion

Well-defined 3 mol% Rh-doped strontium titanate nanocrystals were synthesized by hydrothermal reaction of $Sr(OH)_2$, TiO_2 and $RhCl_3$ in water by modifying the published procedures.[18,49] According to TEM (Fig. 1) and powder X-ray diffraction (Fig. S1, ESI†), the product crystallizes in the perovskite structure type and forms single crystalline cubes with an edge length of 20–75 nm. The perovskite can be modified with Pt or Ru nanoparticles by photodeposition in aqueous H_2PtCl_6 or $RuCl_3$ solution. The Pt forms 2.8 ± 0.4 nm particles (dark dots) randomly on the surface of the Rh:$SrTiO_3$ cubes. The Ru cocatalyst particles are slightly larger (5.3 ± 0.9 nm) and less well-dispersed on the absorber crystals.

Optical spectra of the nanocrystals are shown in Fig. 2. Clearly, Rh introduces a new optical absorption at <500 nm, which causes the yellow (1% Rh) or dark yellow (3% Rh) color of the solid. The absorption is due to the presence of Rh^{3+} t_{2g} states in the band gap of $SrTiO_3$. Interestingly, the characteristic 580 nm absorption of Rh^{4+} in Rh:$SrTiO_3$ particles made by solid state synthesis[36,50,51] is not observed, suggesting that the Rh ions in the nanocrystals are in the +3 oxidation state.

To determine the photocatalytic properties of Rh:$SrTiO_3$ for the visible light driven hydrogen evolution reaction (HER), irradiation experiments were performed in 50 mL of 20 vol% methanol in water (Fig. 3A) as a function of pH (8, 3.5, adjusted with sulfuric acid). Generally the 3% Rh samples yield higher HER rates than the 1% Rh samples, which is a result of improved visible light absorption. Rates were higher in acidic solution

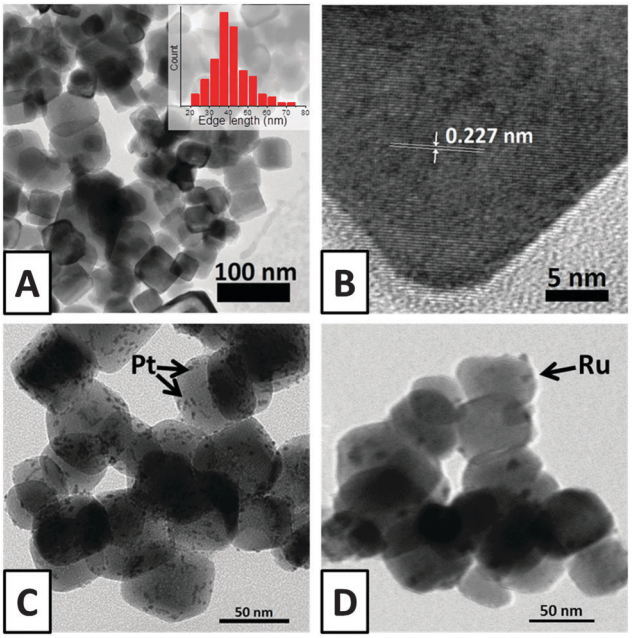

Fig. 1 (A) TEM image with size statistics (inset) and (B) HRTEM image of Rh(3 mol%):$SrTiO_3$ nanoparticles, (C) TEM image of Pt modified Rh(3 mol%):$SrTiO_3$ nanoparticles, and (D) the TEM image of Ru modified Rh(3 mol%):$SrTiO_3$ nanoparticles.

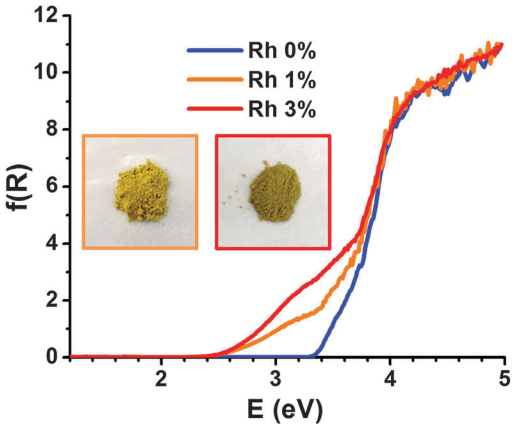

Fig. 2 UV-Vis Spectra with photos of $SrTiO_3$, Rh1%:$SrTiO_3$ (left photo) and Rh(3 mol%):$SrTiO_3$ (right photo). $f(R)$ is proportional to the absorption coefficient. $f(R) = 2R/(1-R)^2$ (Kubelka-Munk function).

(28 μmol g^{-1} h^{-1}) than in basic solution (18 μmol g^{-1} h^{-1}). A further boost of the HER was achieved by the addition of Pt or Ru cocatalysts (Fig. 3B and C). At pH 3.5 the particles produced 68 μmol g^{-1} h^{-1} for the 1% Pt sample and 95 μmol g^{-1} h^{-1} for the 2% Pt sample; Ru cocatalysts generally gave lower rates of 45 μmol g^{-1} h^{-1}. Overall, the H_2 activity of the nanocrystals is lower than the value of 160 μmol g^{-1} h^{-1} for a microcrystalline powder.[36] This is likely a result of the small size of the absorber and reduced electron-hole separation. The HER gain with noble metal cocatalysts is generally attributed to the improved proton reduction kinetics,[46,52] with Ru having approximately 10 times smaller exchange current density ($\log i_0 = -4.2$) for proton reduction than Pt ($\log i_0 = -3.1$).[53,54] However, as we show in

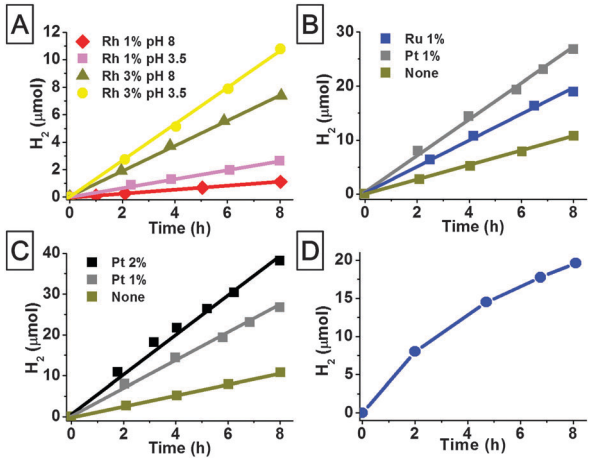

Fig. 3 (A) Visible light driven hydrogen evolution of 1 mol% and 3 mol% Rh-doped $SrTiO_3$ catalysts (50 mg) in 50 mL of 20 vol% MeOH aqueous solution. (B and C) H_2 evolution from 50 mg of 3 mol% Rh-doped $SrTiO_3$ with Pt or Ru cocatalysts in 50 mL of 20 vol% MeOH aqueous solutions at pH 3.5 (adjusted with H_2SO_4). (D) Rh(3 mol%):$SrTiO_3$-Pt(2%) in 0.05 M $K_4Fe(CN)_6$ solution, neutral pH. (A), (B) and (C) were measured under 112 mW cm^{-2} illumination with >400 nm longpass filter and (D) was measured under 380 mW cm^{-2} from 300 W Xe lamp with filter (>400 nm).

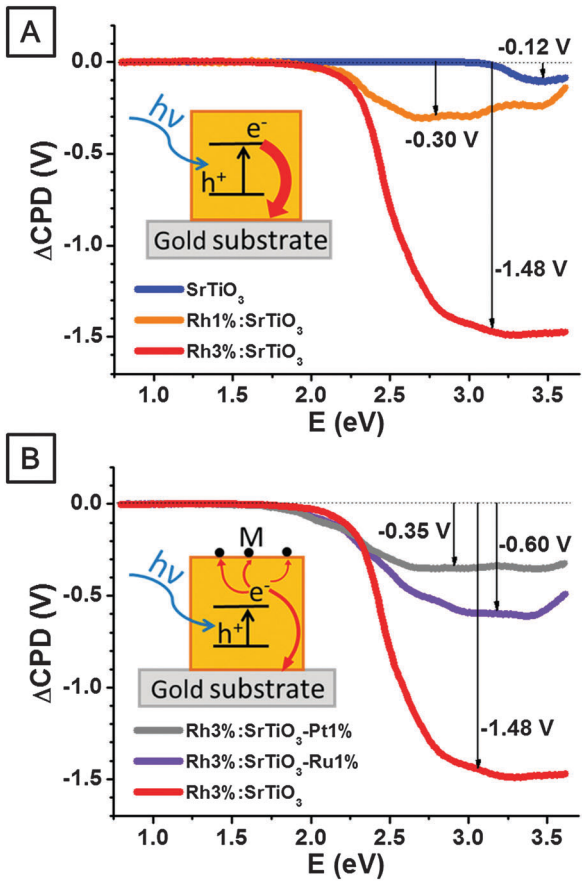

Fig. 4 SPV spectra of (A) doped and non-doped $SrTiO_3$ on gold substrates with schematic mechanism (inset), and (B) Rh(3 mol%):$SrTiO_3$ with 1 wt% Ru or Pt cocatalysts on gold substrates with mechanism scheme (inset).

the following, the metal cocatalysts also contribute to photochemical charge separation at the interface with the absorber.

To measure this effect, surface photovoltage (SPV) spectra were recorded on thin films of the catalysts on a gold substrate (Fig. 4A). In SPS, the variable surface potential of a photocatalyst film is recorded under illumination with variable monochromatic light in the IR to UV range (Fig. S2, ESI†). The sample geometry is shown in Fig. S3 (ESI†). A photovoltage arises from the movement of photogenerated charge carriers through the film or across the film-substrate interface. The spectrum of a Rh:$SrTiO_3$ nanocrystal film is dominated by a negative photovoltage at photon energies above 2.2 eV, the indirect band gap of the material. The negative sign of the voltage is consistent with majority (electron) carrier injection into the FTO substrate, as shown in the inset. In contrast, non-doped $SrTiO_3$ nanocrystals only generate a photovoltage above 3.0 eV. Increasing the Rh content from 1 to 3 mol% magnifies the photovoltage signal from −0.30 V to −1.48 V. The near linear correlation of the 3.0 eV photovoltage size with the Rh content (0, 1, 3 mol%) in the samples demonstrates that the mobile charge carriers in Rh:$SrTiO_3$ originate from excitation of Rh^{3+} t_{2g} states in the lattice. Fig. 4B shows SPV spectra of the noble metal modified 3% Rh nanocrystals. With −0.35 V and −0.60 V, the voltages for the Pt and Ru-modified nanocrystals at 3.0 eV are noticeably smaller than for the pure Rh:$SrTiO_3$ nanocrystals. This is a result of electron transfer to the noble metal nanoparticles (see the inset). Pt particles trap electrons better because the work function (5.4 eV) is higher than that of Ru (4.7 eV). This suggests that electron/hole separation at the Rh:$SrTiO_3$/M nanoparticle interface is controlled by the thermodynamics of the donor-acceptor configuration. Using the photovoltage of the non-modified Rh:$SrTiO_3$ nanocrystals as a reference, the open circuit potential V_{OC} of the metal-absorber junctions can be estimated to be V_{OC}(STO/Pt) = −1.13 V and V_{OC}(STO/Ru) = −0.88 V. This is much below the thermodynamic limit for this configuration, as will be discussed below.

To evaluate photochemical charge transfer at the absorber surface, SPS measurements were repeated after soaking the Rh:$SrTiO_3$ nanocrystal films with dilute solutions of various redox reagents, followed by drying in air. This places the photocatalyst in direct contact with the redox reagents and with their reaction products under illumination, to allow for quasi-equilibrium similar to photocatalytic conditions, despite the lack of a solvent. As can be seen from Fig. 5, the addition of the electron donors KI, $K_4[Fe(CN)_6]$ or methanol boost the voltage of the film by 0.39 V, 0.64 V and 1.16 V (at 3.0 eV), respectively.

This is due to photochemical oxidation of these redox species (see inset) during selective hole transfer from the light absorber. Conversely, the addition $MVCl_2$ or $K_3[Fe(CN)_6]$ reduces the voltage by 1.24 V and 0.73 V, respectively, due to electron injection from the absorber, with concurrent electrochemical reduction of the sacrificial reagents. Using the energy diagram in Fig. 6, the measured open circuit potentials (V_{OC} in brackets) can be related to the built-in potentials V_{bi} of the nanoscale junctions ($eV_{bi} = E_{CB}$(absorber) − E_F(acceptor) for electron transfer and $eV_{bi} = E_{VB}$(absorber) − E_F(acceptor) for hole transfer). For example, electron transfer from Rh:$SrTiO_3$ to the metal cocatalysts is thermodynamically favored, with eV_{bi} (STO/Pt) = −2.3 eV and eV_{bi}(STO/Ru) = −1.4 eV driving

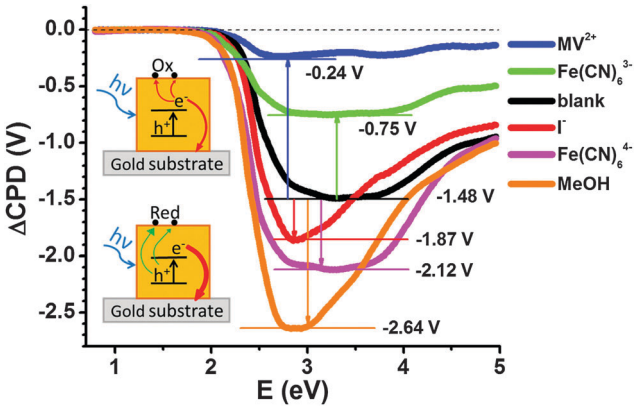

Fig. 5 SPV spectra of 0.5 mg Rh(3 mol%):$SrTiO_3$ on 1 cm^2 gold coated glass in the presence of redox reagents with schematic mechanism (inset). Methanol was added to films as neat liquid and other reagents were added to films as solutions (0.05 mL of 0.01 M) and dried in air.

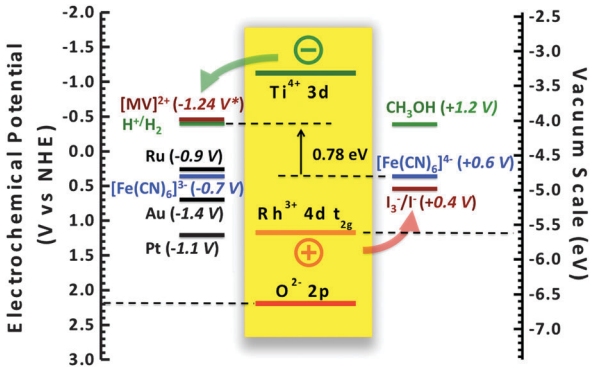

Fig. 6 Energy diagram of Rh:$SrTiO_3$ at pH 7 on electrochemical and vacuum scales, with experimental photovoltages (positive for oxidation, negative for reduction) in brackets. Values for $SrTiO_3$ band edges at the point of zero charge are calculated with the Butler Ginley method.[55,56] The position of the Rh^{3+} t_{2g} states is derived from UV/Vis absorption data. Redox potentials[57] and work functions[58] are from the literature.* The MV^{2+} V_{OC} value is affected by screening (see the text).

force. The observed V_{OC} values are much smaller because electron transfer occurs in competition with hole-transfer from the valence band. Hole injection takes place because the size of the Rh:$SrTiO_3$ nanocrystals is comparable to the hole diffusion length in this material. In contrast, the measured circuit potential V_{OC}(STO/Au) = −1.48 V is much closer to the built-in potential of the Rh:$SrTiO_3$/Au configuration (−1.7 V) because the nanocrystal films (4.4–4.8 μm) filter out the holes from the electrons. This is because the electron diffusion length in $SrTiO_3$ (4.1 μm) is longer than the hole diffusion length (3.3 μm; 0.15 μm for Fe-doped $SrTiO_3$, see ESI† Table S1).

The same considerations govern charge transfer between the nanoscale absorber and the molecular redox reagents. With ferricyanide as a sacrificial electron acceptor, for example, V_{OC}(STO/K_3[Fe(CN)$_6$]) = −0.73 V is observed out of a theoretically possible V_{bi} = −1.42 V. This lower experimental value is due to the proximity of the redox reagent to the absorber, which puts electron donation in competition with hole donation. Another factor is the low intensity of the exciting light beam (0.1 mW cm^{-2} at 3.0 eV), which limits the reducing power (quasi Fermi level) of the light absorber, as explained previously.[25] An unusual situation is encountered with $MVCl_2$ as an electron acceptor. Here, the observed V_{OC} of −1.24 V is larger than the thermodynamic limit V_{bi} = −0.62 V. Tentatively, this discrepancy results from the screening effect of the ions in the films, which attenuate the experimental photovoltage. Further investigations into this important effect are underway. Preferential hole transfer from the Rh:$SrTiO_3$ nanocrystals can be observed in the presence of sacrificial electron donors. Here, it is important to realize that the photoholes are generated under visible light illumination, and thus do not originate from the STO valence band, but from the Ru^{3+} t_{2g} sub band. Then, based on the position of these states, V_{bi}(Rh^{3+}/KI) = +0.6 V, V_{bi}(Rh^{3+}/K_4[Fe(CN)$_6$]) = +0.8 V and V_{bi}(Rh^{3+}/MeOH) = +1.5 V, for hole transfer. Some of the observed photovoltages come quite close to these values. For example, V_{OC} for STO/MeOH of +1.2 V is 80% of the theory. This is because the oxidation of methanol is irreversible. On the other hand, for the STO/KI contact V_{OC} = +0.4 V and for the STO/K_4[Fe(CN)$_6$] contact V_{OC} = +0.6 V. This is within 66% and 75% of the theory, as a result of the more reversible character of these redox reagents. Overall, these experiments establish the oxidative power (oxidation potential) of illuminated Rh:$SrTiO_3$ as +1.5 V *vs.* NHE. Water oxidation at this potential is not achieved because of the slow kinetics of hole transfer to water. However, as the SPS data show, it is enough for the oxidation of ferrocyanide. Indeed, if Rh:$SrTiO_3$/Pt is illuminated in 0.05 M aqueous $K_4Fe(CN)_6$ with visible light (>400 nm), continuous H_2 evolution can be observed (Fig. 3D). The initial rate of 80 μmol g^{-1} h^{-1} approaches that in aqueous methanol despite the lower reducing power and competitive light absorption by ferrocyanide. This is because the illumination power for the ferrocyanide irradiation is much higher (380 instead of 112 mW cm^{-2}). A blank test of the photocatalyst without any sacrificial donor does not lead to hydrogen evolution (Fig. S4, ESI†). These reactions establish Rh:$SrTiO_3$/Pt as truly photosynthetic for the reaction $2\ H^+ + 2\ [Fe(CN)_6]^{4-} \rightarrow 2\ [Fe(CN)_6]^{3-} + H_2$. Based on the energy diagram, approximately 0.78 eV of free energy per absorbed photon are converted into free energy. However, the actual energy conversion is lower, because of the small quantum efficiency of the process (<0.1%). The low quantum efficiency is due to the low visible absorption of the catalyst (see photos in Fig. 2). A higher efficiency might be possible by increasing the Rh^{3+} dopant concentration to above 3 mol%. Also, over time the rate decreases due to competing light absorption of the formed ferricyanide at <500 nm (Fig. S5, ESI†) and because of the back reaction of the catalyst with the oxidized reagent, as evident in the SPS experiment with K_4[Fe(CN)$_6$] in Fig. 5. Nevertheless, the reaction demonstrates that a photosynthetic reaction can be achieved with a transition metal-doped nanoscale absorber.

Experimental

Chemicals

Strontium hydroxide octahydrate (99%, Alfa Aesar), titanium(IV) oxide (Aeroxide P25, Acros organics), titanium(IV) oxide (powder, 99.8%, Aldrich), potassium hydroxide (99.9%, Fisher Scientific),

rhodium(III) chloride hydrate (38–41% Rh, Sterm Chemicals), methanol (99.9%, Fisher Scientific), dihydrogen hexachloroplatinate(IV) hexahydrate (99.9%, Alfa Aesar), ruthenium(III) chloride hydrate (99.9%, Ru 38%, Alfa Aesar), methylviologen dichloride hydrate (98%, Acros Organics), potassium iodide (99.9%, Fisher Scientific), Potassium hexacyanoferrate(III) (99%, Sigma-Aldrich) and Potassium hexacyanoferrate(II) trihydrate (99%, Sigma-Aldrich) were used as received. Water was purified to 18 MΩ cm resistivity by a Nanopure II system.

Synthesis

Rh-doped $SrTiO_3$ nanocrystals were synthesized *via* hydrothermal reactions. To synthesize Rh(1.0 mol%):$SrTiO_3$, 2.25 mmol $Sr(OH)_2$ (0.598 g, 1 mole equiv.) was mixed with 2.23 mmol P25 TiO_2 powder (0.178 g, 99% mole equiv.). Then, 0.0225 mmol $RhCl_3$ (0.00471 g, 1% mole equiv.) was added by adding 4.7 mL 1.0 mg Rh per mL $RhCl_3$ water solution dropwise. 22.5 mmol KOH (1.262 g, 10 mole equiv.) was added afterwards followed by 23 mL pure water, which could fill half of the 45 mL PTFE lined autoclave. After 72 hours at 423 K, a light yellow suspension of Rh(1.0 mol%):$SrTiO_3$ was obtained. In order to remove dissolved starting materials, the suspension was centrifuged and washed with pure water five times until the pH was <8.5. Finally, after the suspension was centrifuged and the solid phase was collected and dried in a vacuum, 0.242 g yellow powder was obtained. The powder can be fully dispersed in water or 20% (v/v) methanol/water solution. The Rh(3.0 mol)%:$SrTiO_3$ nanocrystals were synthesized with the same method, but the amount of P25 TiO_2 powder was decreased to 2.21 mmol (0.175 g, 97% equiv.) and the amount of $RhCl_3$ was increased to 0.0675 mmol (0.0141 g, 3% equiv.) respectively. The Rh(3.0 mol%):$SrTiO_3$ nanocrystals were platinized *via* photo-deposition. 100 mg Rh(3.0 mol%):$SrTiO_3$ was dispersed in 20% (v/v) aqueous methanol solution. To add 1.0 wt% of Pt, 1.0 mL of the H_2PtCl_6 aqueous solution with the concentration of 1.0 mg Pt per mL was added. The mixed solution was stirred in the light of a 300 W Xe lamp (175 mW cm^{-2} at the flask). After photo-deposition, the solution turned from yellow to colorless and the powder from yellow to deep grey. The powder was washed with pure water five times and dried in a vacuum. 70 mg black powder of Rh(3.0 mol%):$SrTiO_3$-Pt(1.0 wt%) was obtained. 2.0 wt% Pt deposition and 1.0 wt% Ru deposition were done with the same method with 2.0 mL of the 1.0 mg Pt per mL H_2PtCl_6 aqueous solution and 1.0 mL of the 1.0 mg Ru per mL $RuCl_3$ aqueous solution, respectively.

Characterization

Transmission electron microscopy (TEM) images were taken using a Philips CM-12 TEM with an accelerating voltage of 120 kV. Bright field high-resolution transmission electron microscopy (HRTEM) images were taken using a JEOL 2500SE HRTEM with an accelerating voltage of 200 kV. To prepare the samples, copper grids with carbon films were dipped into aqueous dispersions of the catalysts, washed with pure water and air dried. Powder X-ray diffraction was conducted with a Scintag XRD at a wavelength of 0.154 nm, with 2 mm tube slit divergence, 4 mm scatter, 0.5 mm column scatter and 0.2 mm receiving widths. The sizes of the nanoparticles were calculated using the Scherrer Equation with five most intense peaks in each diffraction spectrum and averaged. UV-Vis diffuse reflectance spectra were recorded using a Thermo Scientific Evolution 220 Spectrometer. To prepare the samples, the aqueous dispersions of the catalysts were drop-coated on white Teflon tape and then dried in air. The reflectance data were converted to the Kubelka-Munk function as $f(R) = (1 - R)^2(2R)^{-1}$ for scattering correction. Surface Photovoltage Spectroscopy (SPS) measurements were conducted using a vibrating gold Kelvin probe (Delta PHI Besocke) mounted inside a home-built vacuum chamber ($<1 \times 10^{-4}$ mbar). To prepare the samples, 0.1 mL of 5 mg mL^{-1} aqueous dispersions of the catalysts were drop-coated onto gold substrates, dried in air to form thin films of 0.5 mg cm^{-2} and annealed in air at 573 K for 5 h. The thicknesses of the films were 4.4 to 4.8 μm. Samples were illuminated with monochromatic light from a 150 W Xe lamp filtered through an Oriel Cornerstone 130 monochromator (1–10 mW cm^{-2}, for spectrum see Fig. S2, ESI†). The CPD spectra were corrected for drift effects by subtracting a dark scan. Photocatalytic hydrogen evolution tests were performed by dispersing 50 mg of the catalysts in 50 mL of 20 vol% aqueous methanol or 0.05 M $K_4[Fe(CN)_6]$ aqueous solution in a quartz glass flask. The flask was purged with argon and the solution mixture was irradiated with light from a 300 W Xe arc lamp filtered through a 400 nm long pass filter (0.22 M sodium nitrite solution). The power density at the flask was measured using an International Light IL1400BL photometer equipped with a GaAsP detector in the 280 to 660 nm sensitivity range (see Fig. 3 caption). The airtight irradiation system was connected to a Varian 3800 gas chromatograph (with a 60/80 Å molecular sieve column and a thermal conductivity detector) to identify the gas and measure the amount of gas evolved.

Conclusions

In conclusion, we have created well-defined composites of single crystalline 1–3 mol% Rh-doped $SrTiO_3$ nanocrystals and Pt or Ru cocatalysts. Based on optical spectra and SPS, the absorber particles are n-type and Rh is in the +3 oxidation state, contrary to Rh:$SrTiO_3$ made by solid state synthesis.[36,50] Visible light driven H_2 evolution is observed from aqueous methanol and $[Fe(CN)_6]^{4-}$ solutions, supporting a photosynthetic process with 0.78 eV energy deposition per photon in the latter case. For the first time, photovoltage information has become available to gauge photochemical charge separation and junction potentials at the nanoscale. Intermediate potentials of −0.88 to −1.13 V are observed at the absorber – Pt(Ru) interfaces, and large potentials at the absorber – gold interface (−1.48 V). This shows that the Pt and Ru cocatalysts not only improve redox kinetics, but also aid charge separation in the absorber. The selectivity of charge transfer (electron *versus* hole) is controlled by the built-in potentials, the spatial separation between donors and acceptors and by the electron

and hole diffusion length. At a longer distance electron transfer is preferred. Photochemical charge transfer to the molecular redox couples is controlled by the electrochemical potential gradient of the light absorber-acceptor configuration and by the reversibility of the redox couple. These findings provide new insight into the factors that determine the amount of free energy that can be drawn from the nanostructured solar energy conversion devices. They will contribute to the design of more efficient systems for artificial photosynthesis.

Acknowledgements

We thank Prof. Gerd N. Lamar for a generous donation of rhodium chloride and Research Corporation for Science Advancement (Scialog Award) and the National Science Foundation (NSF, Grants 1152250 and 1133099) for financial support.

Notes and references

1 A. Kudo, *MRS Bull.*, 2011, **36**, 32–38.
2 K. Maeda, *J. Photochem. Photobiol., C*, 2011, **12**, 237–268.
3 M. G. Walter, E. L. Warren, J. R. McKone, S. W. Boettcher, Q. X. Mi, E. A. Santori and N. S. Lewis, *Chem. Rev.*, 2010, **110**, 6446–6473.
4 F. E. Osterloh, *Chem. Mater.*, 2008, **20**, 35–54.
5 F. E. Osterloh, *Chem. Soc. Rev.*, 2013, **42**, 2294–2320.
6 P. V. Kamat, K. Tvrdy, D. R. Baker and J. G. Radich, *Chem. Rev.*, 2010, **110**, 6664–6688.
7 M. B. Wilker, K. J. Schnitzenbaumer and G. Dukovic, *Isr. J. Chem.*, 2012, **52**, 1002–1015.
8 J. Wang and F. E. Osterloh, *J. Mater. Chem. A*, 2014, **2**, 9405–9411.
9 R. Abe, *J. Photochem. Photobiol., C*, 2010, **11**, 179–209.
10 F. E. Osterloh, *Top. Curr. Chem.*, 2015, DOI: 10.1007/128_2015_633.
11 F. E. Osterloh, *J. Phys. Chem. Lett.*, 2014, **5**, 2510–2511.
12 B. Klahr, S. Gimenez, F. Fabregat-Santiago, T. Hamann and J. Bisquert, *J. Am. Chem. Soc.*, 2012, **134**, 4294–4302.
13 S. Ida, A. Takashiba, S. Koga, H. Hagiwara and T. Ishihara, *J. Am. Chem. Soc.*, 2014, **136**, 1872–1878.
14 A. J. Nozik and R. Memming, *J. Phys. Chem.*, 1996, **100**, 13061–13078.
15 R. Memming, *Top. Curr. Chem.*, 1994, **169**, 105–181.
16 F. D. Lin and S. W. Boettcher, *Nat. Mater.*, 2014, **13**, 81–86.
17 M. Waller, T. K. Townsend, J. Zhao, E. M. Sabio, R. L. Chamousis, N. D. Browning and F. E. Osterloh, *Chem. Mater.*, 2012, **24**, 698–704.
18 T. K. Townsend, N. D. Browning and F. E. Osterloh, *ACS Nano*, 2012, **6**, 7420–7426.
19 L. Kronik and Y. Shapira, *Surf. Sci. Rep.*, 1999, **37**, 1–206.
20 L. Kronik and Y. Shapira, *Surf. Interface Anal.*, 2001, **31**, 954–965.
21 T. K. Townsend, N. D. Browning and F. E. Osterloh, *Energy Environ. Sci.*, 2012, **5**, 9543–9550.
22 F. E. Osterloh, M. A. Holmes, L. Chang, A. J. Moule and J. Zhao, *J. Phys. Chem. C*, 2013, **117**, 26905–26913.
23 R. Beranek, B. Neumann, S. Sakthivel, M. Janczarek, T. Dittrich, H. Tributsch and H. Kisch, *Chem. Phys.*, 2007, **339**, 11–19.
24 D. Gross, I. Mora-Sero, T. Dittrich, A. Belaidi, C. Mauser, A. J. Houtepen, E. Da Como, A. L. Rogach and J. Feldmann, *J. Am. Chem. Soc.*, 2010, **132**, 5981–5983.
25 J. Zhao and F. E. Osterloh, *J. Phys. Chem. Lett.*, 2014, **5**, 782–786.
26 F. A. Frame, T. K. Townsend, R. L. Chamousis, E. M. Sabio, T. Dittrich, N. D. Browning and F. E. Osterloh, *J. Am. Chem. Soc.*, 2011, **133**, 7264–7267.
27 M. K. Nowotny, P. Bogdanoff, T. Dittrich, S. Fiechter, A. Fujishima and H. Tributsch, *Mater. Lett.*, 2010, **64**, 928–930.
28 P. Zabel, T. Dittrich, M. Funes, E. N. Durantini and L. Otero, *J. Phys. Chem. C*, 2009, **113**, 21090–21096.
29 J. G. Mavroides, J. A. Kafalas and D. F. Kolesar, *Appl. Phys. Lett.*, 1976, **28**, 241–243.
30 M. S. Wrighton, A. B. Ellis, P. T. Wolczanski, D. L. Morse, H. B. Abrahamson and D. S. Ginley, *J. Am. Chem. Soc.*, 1976, **98**, 2774–2779.
31 K. Domen, S. Naito, M. Soma, T. Onishi and K. Tamaru, *J. Chem. Soc., Chem. Commun.*, 1980, 543–544.
32 Z. B. Jiao, Y. Zhang, T. Chen, Q. S. Dong, G. X. Lu and Y. P. Bi, *Chem. – Eur. J.*, 2014, **20**, 2654–2662.
33 A. Kudo and Y. Miseki, *Chem. Soc. Rev.*, 2009, **38**, 253–278.
34 H. Kato and A. Kudo, *J. Phys. Chem. B*, 2002, **106**, 5029–5034.
35 T. Ishii, H. Kato and A. Kudo, *J. Photochem. Photobiol., A*, 2004, **163**, 181–186.
36 R. Konta, T. Ishii, H. Kato and A. Kudo, *J. Phys. Chem. B*, 2004, **108**, 8992–8995.
37 H. Kato, Y. Sasaki, N. Shirakura and A. Kudo, *J. Mater. Chem. A*, 2013, **1**, 12327–12333.
38 R. Niishiro, H. Kato and A. Kudo, *Phys. Chem. Chem. Phys.*, 2005, **7**, 2241–2245.
39 S. X. Ouyang, H. Tong, N. Umezawa, J. Y. Cao, P. Li, Y. P. Bi, Y. J. Zhang and J. H. Ye, *J. Am. Chem. Soc.*, 2012, **134**, 1974–1977.
40 Y. Sasaki, H. Nemoto, K. Saito and A. Kudo, *J. Phys. Chem. C*, 2009, **113**, 17536–17542.
41 Q. Jia, A. Iwase and A. Kudo, *Chem. Sci.*, 2014, **5**, 1513–1519.
42 K. Maeda, *ACS Catal.*, 2013, **3**, 1486–1503.
43 A. Iwase, Y. H. Ng, Y. Ishiguro, A. Kudo and R. Amal, *J. Am. Chem. Soc.*, 2011, **133**, 11054–11057.
44 H. Kato, M. Hori, R. Konta, Y. Shimodaira and A. Kudo, *Chem. Lett.*, 2004, **33**, 1348–1349.
45 H. Kato, Y. Sasaki, A. Wase and A. Kudo, *Bull. Chem. Soc. Jpn.*, 2007, **80**, 2457–2464.
46 Y. Sasaki, A. Iwase, H. Kato and A. Kudo, *J. Catal.*, 2008, **259**, 133–137.
47 R. Marschall, *Adv. Funct. Mater.*, 2014, **24**, 2421–2440.
48 T. Hisatomi, J. Kubota and K. Domen, *Chem. Soc. Rev.*, 2014, **43**, 7520–7535.
49 T. Tsumura, K. Matsuoka and M. Toyoda, *J. Mater. Sci. Technol.*, 2010, **26**, 33–38.

50 K. Iwashina and A. Kudo, *J. Am. Chem. Soc.*, 2011, **133**, 13272–13275.
51 R. Konta, T. Ishii, H. Kato and A. Kudo, *J. Phys. Chem. B*, 2004, **108**, 8992–8995.
52 J. M. Lehn, J. P. Sauvage and R. Ziessel, *New J. Chem.*, 1980, **4**, 623–627.
53 S. Trasatti, *J. Electroanal. Chem.*, 1972, **39**, 163–184.
54 C. C. L. McCrory, S. Jung, I. M. Ferrer, S. M. Chatman, J. C. Peters and T. F. Jaramillo, *J. Am. Chem. Soc.*, 2015, **137**, 4347–4357.
55 M. A. Butler and D. S. Ginley, *J. Electrochem. Soc.*, 1978, **125**, 228–232.
56 Y. Xu and M. A. A. Schoonen, *Am. Mineral.*, 2000, **85**, 543–556.
57 P. Vanysek, *CRC Handbook of Chemistry and Physics*, CRC Press/Taylor and Francis, Boca Raton, FL, 88 (internet version 2008) edn, 2008.
58 D. R. Lide, *CRC Handbook of Chemistry and Physics*, CRC Press/Taylor and Francis, Boca Raton, FL, 88 (internet version 2008) edn, 2008.

